Title	Predictions of ICHAZ cyclic thermo-mechanical response in GTAW process for 9Cr steels
Author(s)	Mac Ardghail, Padraig; Barrett, Richard A.; Harrison, Noel M.; Leen, Sean B.
Publication Date	2019-02-25
Publication Information	Mac Ardghail, Padraig, Barrett, Richard A., Harrison, Noel, & Leen, Sean B. (2019). Predictions of ICHAZ Cyclic Thermomechanical Response in GTAW Process for 9Cr Steels. Journal of Pressure Vessel Technology, 141(2). doi: 10.1115/1.4042712
Publisher	ASME The American Society of Mechanical Engineers
Link to publisher's version	https://doi.org/10.1115/1.4042712
Item record	http://hdl.handle.net/10379/15685
DOI	http://dx.doi.org/10.1115/1.4042712

PREDICTIONS OF ICHAZ CYCLIC THERMO-MECHANICAL RESPONSE IN GTAW PROCESS FOR 9CR STEELS

Padraig Mac Ardghail
Mechanical Engineering and Ryan Institute, NUI Galway, Ireland
Alice Perry Engineering Building, NUI Galway, University Road, Galway, Ireland
p.macardghail1@nuigalway.ie

Richard A. Barrett
Mechanical Engineering and Ryan Institute, NUI Galway, Ireland
Alice Perry Engineering Building, NUI Galway, University Road, Galway, Ireland
richard.barrett@nuigalway.ie

Noel Harrison
Mechanical Engineering and Ryan Institute, NUI Galway, Ireland
Alice Perry Engineering Building, NUI Galway, University Road, Galway, Ireland
noel.harrison@nuigalway.ie

Sean B. Leen
Mechanical Engineering and Ryan Institute, NUI Galway, Ireland
Alice Perry Engineering Building, NUI Galway, University Road, Galway, Ireland
sean.leen@nuigalway.ie

ABSTRACT

This work is concerned with the development of a modelling framework to predict the effects of tempered-untempered martensite heterogeneity on the thermo-mechanical performance of welded material. A physically-based visco-plasticity model for the inter-critical heat-affected zone (ICHAZ) for 9Cr steels (e.g. P91, P92) is presented in this work, with the ICHAZ represented as a mixture of tempered and untempered martensite. The constitutive model includes dislocation-based Taylor hardening and damage for different material phases. A sequentially-coupled thermal-mechanical welding simulation is conducted to predict the volume fraction compositions for the various weld-affected material zones in a cross-weld specimen. The out-of-phase cyclic thermo-mechanical (25^{o}C to 600^{o}C) performance of notched and plain samples is comparatively assessed for a range of different tempered-untempered martensitic material heterogeneities. It is shown that the heterogeneity in a simulated cross-weld material is highly detrimental to thermal cyclic performance.

INTRODUCTION

Modern power generation requires ever greater efficiency to reduce carbon emissions, reduce fuel costs and to reduce pollution. This can be done by utilizing renewable or clean energy sources such as wind energy. However, wind energy storage is difficult, so power is only generated when weather conditions are favourable, otherwise conventional power plant is required. This results in fluctuating-output operation for thermal power plant, to compensate for inconsistent renewable energy sources, known as load-following operation. Greater efficiency is also obtained in thermal power plant by increasing the plant operating temperatures and steam pressures [1]. Current state-of-the-art power plant operates under ultra-supercritical (USC) conditions.

USC and load-following operation result in increased creep loading, thermo-mechanical fatigue and creep-fatigue of power-plant components. USC operation, in particular, creates the additional problem of operating temperatures exceeding the design temperatures of current power plant components, primarily composed of 9Cr steels such as P91 or P92 [2]. Load-following operation can cause failure in welded components even without exceeding the design temperatures of the material due to the introduction of thermomechanical fatigue (TMF) loading, e.g. the temperature and stress-strain conditions vary simultaneously.

9Cr steels are high-temperature martensitic steels with carbide precipitate nano-strengthening [3]. These steels are strong due to high-dislocation-density in the martensitic laths but they soften as their dislocation-density reduces. In 9Cr steels, such

as P91, this is due to strain-softening. Strain encourages dislocation-slip, which leads to the annihilation of dislocations.

9Cr steels maintain their dislocation-density at high temperatures via their hierarchical microstructure, which prevents dislocation motion, annihilation and softening. This consists of high- angle boundary prior-austenite grains (PAG) and high-angle boundary packets. Each packet contains blocks, which in turn contain high dislocation-density martensitic laths. The laths contain fine MX precipitates, solutes and larger $M_{23}C_6$ carbides [3-6]. The high-angle boundaries, carbides and precipitates retard dislocation motion and maintain strength [4, 5].

Welding subjects the local material to high temperatures and heating rates, compromising the microstructure in the heat-affected zone (HAZ) and weakening it. Failure of plant components most often occurs in the inter-critical HAZ (ICHAZ) or in the adjacent fine-grained HAZ (FGHAZ), which is known as Type IV cracking. Type IV cracking is essentially a creep-dominated failure but research suggests that high-temperature fatigue will also produce failure in the IC-FGHAZ, similar to Type IV [7, 8]. For this work, the area of interest is the ICHAZ and understanding its behavior.

During welding, the ICHAZ partially transforms from parent metal (PM) martensite to austenite. These austenite grains become PAGs after the material cools and returns to martensite. The ICHAZ PAGs are detrimental to creep properties because, due to recrystallization, they are much smaller than PM PAGs. At the same time, carbides, especially $M_{23}C_6$, coarsen at high temperature [9], which makes them less effective at preventing dislocation motion. Recrystallisation will create new grain

boundaries without any $M_{23}C_6$ [10], so these boundaries are weaker. When $Cr_{23}C_6$ carbides dissolve, this raises the local austenite transformation start temperature, A_{c1}, so no austenite transformation occurs, which can then lead to retained ferrite after cooling [11]. At the same time, smaller austenite grains may not transform back to martensite but rather become retained austenite [12]. Retained austenite and ferrite lack hierarchical microstructures and are weak at high temperatures. All of this creates the conditions for early failure, which comes as Type IV cracking.

One solution is to design a new material for power plant where the HAZ microstructure does not radically change compared to the PM during welding. This can be achieved by the addition of Boron to 9Cr steels and a new candidate material, MarBN, is currently under review [10, 13]. However, power plant operators have limited scope to adopt a new, untried material in favour of better established 9Cr steels due to industry standards and codes restrictions. Therefore, improving the welding process to preserve the ICHAZ is an attractive proposition.

This work seeks to compare the response of the ICHAZ to PM and FGHAZ responses under TMF loading conditions in order to better understand the mechanical response as a first step towards improving the ICHAZ strength. TMF loading is of particular importance because it has been shown to lead to significantly early failure relative to isothermal high-temperature fatigue for 9Cr steel [14]. Power plant components have been shown to fail under load-following conditions (which introduce aspects of TMF loading) e.g. a tee-joint that failed in under 10,000 hours of service [15].

An ICHAZ region is produced using a sequentially-coupled thermal and structural analysis, using a similar approach to the work of Yaghi et al. [16]. The constitutive response of the material was modelled and calibrated against test data [17]. The material model defines two sub-phases of 9Cr steel, tempered and untempered martensite, which represent the PM and the as-welded FGHAZ, respectively. This material model is implemented using a rule-of-mixtures approach, where the ICHAZ material is a mixture of tempered and untempered martensite sub-phases.

Methodology

A key component of the through-process methodology presented here is a sequentially-coupled thermal-mechanical model of the GTAW process, similar to [16], to predict the welding-induced solid-state phase distributions in the PM and HAZ. This was implemented using the commercial finite-element (FE) software, Abaqus. The thermal analysis in [16] applied a body heat-flux to different weld beads in a welding simulation. In the present work, the welding thermal load is defined via a time-dependent temperature boundary condition (see [18] for further details). The boundary-condition heated selected PM material up to 1050^{o}C in 0.1 s, held the temperature at 1050^{o}C for 0.1s and then allowed to cool according to the heat-transfer properties described in [16], with an ambient temperature of 20^{o}C. The element-type was CAX8R for the thermal analysis. The model was axisymmetric. The element size was approximately 0.1 mm.

The subsequent mechanical analysis uses the resulting transient temperature field along with temperature-dependent mechanical properties for stress-strain analysis of the welding process. The mesh was identical in order to match the positions of elemental nodes but the element type was DCAX8. For notched specimens, mesh sensitivity was conducted by examining the maximum in-plane strain at various locations in the notched specimen. A reduction in element size by a factor of 3 resulted in a 1% change in the strain results, so the mesh was considered converged.

The ICHAZ is a region which partially transforms from PM tempered martensite to austenite and subsequently to untempered martensite, leaving the ICHAZ as a mixture of soft (tempered martensite, PM) and hard material (untempered martensite). Figure 1 shows the continuous-cooling-transformation diagram for 9Cr steels [19, 20]. For this work, due to the rapid cooling associated with the GTAW process for the component sizes of interest (typically about 1200 s) and by reference to Fig. 1, it is clear that no ferrite or austenite should form in the HAZ region. This idealization is motivated by the as displayed in Fig. 1.

The through-process welding simulation tool is applied here to a PM specimen to transform it into a cross-weld (CW) specimen, thus providing a test coupon representation of the critical HAZ-PM interface inhomogeneous region, for subsequent thermal fatigue analysis and assessment. The specimen represented a CW specimen extracted from a welded joint, as illustrated in Fig. 2. In Fig. 2b, the dimensions of the specimen in question are shown. Only one end of the specimen is heated according to the aforementioned temperature boundary-condition. This creates a specimen where

one end is untempered martensite, the opposite end remains tempered PM and an ICHAZ forms to separate the different regions. This specimen represents the implementation of a through-process methodology, from a welding process to service conditions.

The structural analysis is conducted using an original constitutive model, which also predicts the evolution of solid-state phases in the material during the welding process.

In the case of the CW specimen, the mixture of tempered and untempered martensite in the ICHAZ is defined by the temperature history. When the material heats up, the material transforms from tempered martensite to austenite. The austenite volume fraction is defined as:

$$V_f = 1 - \frac{A_{c3} - T}{A_{c3} - A_{c1}} \tag{1}$$

where V_f is the volume fraction of austenite, T is the current temperature, A_{c1} is the temperature at which martensite begins to transform to austenite and A_{c3} is the temperature at which martensite completes austenitic transformation. When the material cools, the austenite transforms to untempered martensite according to:

$$V_f = 1 - \frac{T - M_f}{M_s - M_f} \tag{2}$$

where V_f is the volume fraction of untempered martensite, M_s is the temperature at which austenite begins to transform to martensite and M_f is the temperature at which austenite completes martensitic transformation. The values of these transformation

temperatures are shown in Table 1. The method by which the phase volume fractions are calculated is shown in Fig. 3.

Each solid state sub-phase, tempered and untempered martensite, is calibrated separately against material test data from [17]. A unified viscoplastic material model, similar to that of [21], but adapted for anisothermal (welding and TMF) conditions and with a different damage formulation, is implemented here for the welding and post-weld simulations. The flow-rule is given by:

$$\dot{\varepsilon}_p = \alpha \sinh\left(\beta\left(\frac{\sigma}{1-D} - R - \sigma_y\right)\right) \tag{3}$$

where α and β are defined as:

$$\alpha = \varphi_1 e^{\varphi_2 T} \tag{4}$$

$$\beta = \varphi_3 e^{\varphi_4 T} \tag{5}$$

Stress is updated via Hooke's law:

$$\dot{\sigma} = E\left(\dot{\varepsilon} - \dot{\varepsilon}_p\right) \tag{6}$$

Physically-based isotropic hardening is incorporated via a Taylor hardening form, as follows:

$$\dot{R} = \frac{B\dot{\bar{\rho}}}{\sqrt{\bar{\rho}}} \tag{7}$$

based on normalized dislocation density, defined as:

$$\bar{\rho} = \frac{\rho - \rho_i}{\rho} \tag{8}$$

Here ρ is the current dislocation density and ρ_i is the initial dislocation density. Thus the normalized dislocation density starts at 0 ($\rho = \rho_i$) and approaches 1 in the limit as $\rho \to \infty$. Normalised dislocation density is a convenient variable to use because dislocation density is difficult to measure. The evolution of dislocation density is defined as:

$$\dot{\bar{\rho}} = c_1(1-\bar{\rho})\left|\dot{\varepsilon}_p\right| - c_2\bar{\rho} \tag{9}$$

The first term represents dislocation density accumulation during plastic deformation and the second term represents recovery which reduces dislocation density. In the Taylor hardening equation, Equation 7, B is defined as:

$$B = \frac{\alpha_g M G\sqrt{b}}{\sqrt{KL}} \tag{10}$$

where α_g is a multiplicative constant; M is the Taylor factor; G is the shear modulus of the material; b is the magnitude of the Burgers vector; K and L are dislocation recovery rate and mean dislocation path length [22]. A Taylor hardening model is adopted, rather than a Chaboche-type [23], due to the importance of dislocation density for physically-based softening of 9Cr steels [4, 24].

Damage is modelled to account for necking (under tensile loading) and failure of the material. Following [21], the damage is calculated using two variables, one for damage nucleation and the other for damage cavitation:

$$\dot{\omega}_1 = a_1\dot{\bar{\rho}} \tag{11}$$

$$\dot{\omega}_2 = \frac{a_2\left|\dot{\varepsilon}_p\right|}{(1-D)^x} + \frac{a_3\left|\dot{\varepsilon}_p\right|}{(1-D)^y} \tag{12}$$

D is the total damage, described by addition of nucleation and propagation damage terms:

$$\dot{D} = \dot{\omega}_1 + \dot{\omega}_2 \tag{13}$$

Damage modelling is necessary to allow material softening in the material model. Dislocation-density recovery in Equation 4 only limits hardening, rather than softening the material. Physically, Equation 11 represents micro-cracking caused by dislocation motion and Equation 12 represents the coalescence and propagation of these micro-cracks. For modelling purposes, a critical value for damage was defined as 0.6. It is clear from Figs. 6 and 7 that when the material has incurred 60% damage, the amount of additional strain necessary to reach 100% damage is negligible. Therefore, there is no advantage to setting a critical damage threshold above 0.6 while at the same time, the threshold of 0.6 averts the possibility of the damage reaching or exceeding a value of 1, which would cause mathematical errors. When a finite element reaches the critical damage threshold, it is redefined as a soft material with an elastic modulus of 100 MPa. This reduces the load-bearing capacity of the 'failed' element and redistributes the load to undamaged regions.

The material constants M, b, K and L are all physical constants, obtained from literature [22] and displayed in Table 2. A Poisson's ratio of 0.3 was assumed.

Equations 3 to Equation 13 are solved implicitly by a Newton iterative solution, since there is co-dependency between many variables, e.g. plastic strain and damage, which both appear in Equation 3 and Equation 12.

The temperature-dependent material parameters α, β, a_1, a_2, a_3, c_1, c_2, x and y are identified by an iterative minimization-of-errors process for austenite, tempered martensite and untempered martensite, at a range of temperatures from 20°C to 850°C.

The first constants to be identified are α and β, derived from the uniform elongation region of the stress-strain curves at various temperatures. The next variable to be identified is c_1, to match the initial hardening of the material. Different values of c_1 were found for different temperatures and the maximum value across these temperatures was chosen. This led to an exaggerated hardening rate for temperatures above and below the temperature to which c_1 corresponded. At lower temperatures, the damage variable a_1 is identified to restore the hardening rate by accounting for micro-cracking in a harder material. The variable c_2 is identified at higher temperatures to account for dislocation-density recovery, which does not occur at low temperatures. Next to be identified are a_2 and x to account for necking, with a_3 and y identified in order to capture failure. The identification was done at a range of discrete temperatures, using linear interpolation for intermediate temperatures.

Previous work by the authors [18] implemented a rule-of-mixtures approach at single material points when predicting the ICHAZ response. All modelling constants were weighted according to the volume fractions of tempered and untempered martensite. The current work improves upon this by (i) implementing the material model as an Abaqus user-material (UMAT) subroutine, which enables multi-axial analysis and (ii) including the austenite (during welding, above A_{c1}) as a third phase also. It also enables analysis of a cross-weld specimen, which includes a full ICHAZ region, with a range of

volume fractions of tempered and untempered martensite (and austenite during welding). Figure 4 shows a flowchart of how the model operates post-welding, from parameter definition for tempered or untempered martensite, through the rule-of-mixtures parameter assignment and Newton-Raphson iterative calculations. For simplicity, the uniaxial form of the code is shown.

The simulation, described schematically in Figure 5, is conducted on an axisymmetric cross-section, 1 mm in radius and 2 mm high, representing a solid cylindrical component. This small geometry is selected for expediency because it would cool rapidly in a simulation due to its small size.

Both notched and unnotched geometries were investigated. In a welded joint, notches may appear in the form of welding defects. This is especially important for the untempered martensite material, which is adjacent to the WM and thus more likely to include defects caused by the welding process. The set of simulated specimens is described in Table 3.

The geometry was loaded using a cyclic temperature, applied as a time-dependent boundary condition with temperature varying between 25^{o}C and 600^{o}C, with triangular waveform (Fig. 5). This loading represents an idealization of load-following temperature cycles in power-plant, from room temperature to service temperature, although the heating rates are exaggerated for expediency of simulation.

The period of each thermal cycle is 12s. In order to create stress on the material, the geometry is constrained on the top and bottom surfaces, fixing them as though the material were clamped. Physically this can represent a pipe section, for example, with

constrained ends. The loading experienced by the material corresponds to out-of-phase thermo-mechanical fatigue.

RESULTS

The Abaqus UMAT is calibrated against literature test data [17] for all three phases. The results of this calibration for tempered and untempered martensite are displayed in Figs. 6 and 7; similar correlation was achieved for austenite. The full list of identified material constants is given in Tables 4 to 6. It is clear from Figs. 6 and 7 that the untempered martensite has a higher yield stress than the tempered martensite for all temperatures within the TMF range applied in this work. Note that Figs. 6 and 7 display engineering stresses and strains. This calibrated material model is applied to the thermal loading simulation. The results of various simulated cases are summarized in Table 3.

Figures 8, 9 and 10 display the influence of tempered-untempered martensite volume fraction on stress-temperature response. A tendency towards elastic shakedown is visible with increasing untempered martensite volume fraction. As the untempered martensite volume fraction increases, so does the yield stress until the TMF temperature range is no longer enough to cause yield to occur. However, even though the 80% tempered (Case 4 in Table 3) sample, representing ICHAZ, had a higher yield stress than the PM (Case 1 in Table 3) sample, it failed after fewer cycles.

In Figure 11, the CW specimen is compared to the PM (tempered martensite) specimen. The initial response of the CW sample is similar to the PM (Case 1). This

similarity was also observed for strain-controlled cyclic behaviour [7]. This is attrributed due to the iso-stress condition, where the bulk response is controlled by the softest material region, in this case the PM (tempered martensite).

Figure 12 shows the weld life reduction factor $\left(WLRF = {N_f}^{PM}/{N_f}^{CW}\right)$ for isothermal HTLCF cases [7] at 400°C and 500°C as well as the predicted relative life for the CW specimen in the current work. The solid lines project forward to 600°C, which was the peak temperature in the current work. The predicted WLRF for this work is higher than the projections from the test data but this is to be expected of TMF compared to HTLCF. TMF was shown to lead to lower life than HTLCF by a factor of approximately 1.33 at 600°C [14]. This adjustment was applied to the model results and shows consistency with the HTLCF trends.

Figures 13 and 14 show results for notched specimens of tempered and untempered martensite, respectively, showing the influence of increasing notch size on stress-temperature response. The introduction of a notch leads to a dramatic, detrimental effect on life (see Table 3). The effect of introducing a notch was more significant for the untempered material.

The local stress, strain and damage evolutions are displayed in Fig. 15 for the tempered, notched sample (Case 3 in Table 3). It is clear that the damage initiates at the notch root and then spreads into the material, resembling a crack. This was the general trend for each of the notched samples.

Figure 16 displays the evolution of temperature, tempered martensite volume fraction and normalized dislocation density during the heating phase of the welding in

the CW specimen, demonstrating welding-induced constitutive behaviour. The dislocation-density evolution is more dramatic at the free surface of the specimen. One end of the specimen is rapidly heated, leading to a thermal gradient with an associated strain-gradient due to expansion. This gradient introduced more severe multi-axial strain at the free edge compared to the core, thus creating more severe plastic deformation and dislocation-density evolution.

DISCUSSION

The results of this study predict failure in the ICHAZ, consistent with previous work [2]. It appears qualitatively that the untempered material is significantly stronger than the tempered material in TMF, but that it is also significantly more sensitive to the presence of notches.

The constitutive model utilized in this work has been successfully calibrated against monotonic data for 9Cr steel at a wide range of temperatures for PM (Figure 6), austenite (not shown here) and untempered martensite (Figure 7); the latter represents as-welded FGHAZ. It is assumed that the monotonic material response, e.g. the elastic and post-yield response, can be taken as a reasonable approximation of the cyclic behaviour of the various material phases, to allow demonstration of the proof-of-concept of the through-process methodology, in the absence of cyclic data for untempered martensite (from welding) and austenite. Ongoing work is focused on thermo-mechanical physical simulation testing (Gleeble) to generate HAZ material for cyclic testing and calibration. This will be reported on in due course. The model permits the modelling of

anisothermal, mixed-phase constitutive material response which is necessary for through-process simulation and cyclic thermo-mechanical response.

Table 3 indicates that the ICHAZ, represented by Case 4, is the weakest single region of the weld joint, consistent with [2]. Case 4 had fewer cycles to failure compared to Case 1. The ability of the model to capture this phenomenon is due to the rule-of-mixtures method for the dual-phase material. Small increases in untempered martensite significantly increase the dislocation-density evolution rate (Eqn. 9) and thus the damage initiation rate (Eqn. 11). This early damage of ICHAZ regions was found in [18] for tensile loading and demonstrates the advantage of the rule-of-mixtures method over the iso-stress or iso-strain approaches when dealing with hard and soft material mixtures.

Although the rule-of-mixtures approach is an idealized method to capture the principle of a mixed-phase region, here the ICHAZ, it is a simple and convenient method and gives results, here, which qualitatively correspond to experimentally-observed trends. An alternative to rule-of-mixtures is to use micro-mechanical modelling to partition the geometry into discrete tempered and untempered regions, to better capture localized heterogeneous behaviour, with untempered islands surrounded by a softer, tempered matrix, as observed in [25]. However, this would typically preclude modelling of a macro-scale specimen such as the CW specimen, as achieved in the present work, due to computational overhead and model size.

The CW specimen had a much reduced life compared to the PM sample (Case 1) due to welding-induced damage. Figure 16 reveals dislocation-density evolution during

welding due to high-temperature plasticity. This initiates damage in the CW specimen, which TMF loading then causes to propagate, leading to early failure. This demonstrates that welding-induced heterogeneous damage in welded joints is a dominant factor relative to the composition of separate regions (cf. Figs 8, 9 and 10).

The results in Table 3 demonstrate that the presence of a notch is detrimental to material strength. A relative notch size of 1% significantly reduced specimen life for both tempered and untempered martensite specimens, especially untempered martensite. Larger notches further reduced predicted TMF life. The analysis of notches was concerned with the notch radius relative to the specimen thickness, so a larger specimen would have been modelled with larger notches and the authors expect this would have produced similar trends to those witnessed.

The geometry used in this work, a 2 mm high section with a 1 mm radius, is a simplification of tensile specimens extracted from welded joints [7]. The authors considered that any additional geometry height would only add material remote from the region of interest (the ICHAZ in a CW specimen, or a notch). Physically, a CW specimen would straddle the ICHAZ seen in Figure 2a, while a homogeneous specimen would not.

The assumption of the ICHAZ consisting only of tempered and untempered martensite is an idealization, but is reasonable for the material in question, 9Cr steel. Another material, such as SA508, would require a more sophisticated means of defining the HAZ since SA508, for example, can form mixtures of ferrite, pearlite, bainite and martensite, depending on the cooling rate [26]. Equations 1 and 2 in this work are

similar to the martensitic transformation equation used in [26]. The other equations in [26] pertain to ferrite, pearlite and bainite formation, none of which are considered in this work. Neither Equations 1 nor 2 include time dependence. This is due to the rapid transformation during heating and due to the nominal presence of only martensite upon cooling as indicated in Figure 1.

Equations 1 and 2 differ from transformation equations utilized by Yaghi et al. [17] (Koistinen and Marburger (KM) [27]). The authors considered the linear equations to be sufficient for the present work. Volume changes caused by phase-transformation (contraction during martensite-to-austenite, expansion during austenite-to-martensite) are not considered in this work. Since the transformation in the current work neglects volume-changes, the transformation-rate is less important. Non-linear equations would produce different strain-temperature results compared to linear equations but since this work does not consider volume-changes, linear equations were sufficient. The emphasis of this work is the development of a through-process methodology. Future work will refine the model to include volume changes as well as other microstructure evolutions, such as PAG size, laths, precipitates, etc. Other work by the authors [28] incorporated the K-M equation and volume-changes and the effect on the key parameters for this work (post-weld dislocation-density), were not found to be significant.

For homogeneous, untempered martensite specimens, it is assumed that the effects of phase transformation are implicit in the identified mechanical properties of untempered martensite (Table 4). The untempered martensite has a higher yield stress than when tempered, particularly at lower temperatures. The higher yield stress is

associated with a higher dislocation-density. The dislocation-density is higher due to distortions in the crystal structure caused by excess trapped carbon atoms. Higher carbon content increases martensite hardness [29] and therefore yield stress. During tempering, some of this carbon would form precipitates or otherwise diffuse out of the crystal structure, relieving the distortions, reducing dislocation-density and softening the material.

The work presented corresponds to an as-welded joint. The tempering of untempered regions, either due to multi-pass welding as in [17], or due to PWHT, will be examined in future work. The use of the material thermal properties from [16] together with Equations 1 and 2 produced a reasonable means of creating a CW specimen. For the CW specimen, the untempered martensite and mixed-phase ICHAZ regions are generated without transformation plasticity and thus without residual stress. The expected effect of the inclusion of residual stress is a reduction in the stress range for the CW specimen in Fig. 11 due to (a) the residual stresses causing yield after less applied stress and (b) welding-induced damage caused by transformation plasticity in conjunction with Eqn. 11. The welding induced damage may also have reduced the number of cycles to failure for the CW specimen (Table 3) but this would not have changed the main findings of the work presented here. The emphasis of this work was the development of a through-process methodology, from welding to microstructure evolution to mechanical performance, rather than predicting residual stress.

The cyclic period of the thermal load was 12 seconds. Real plant start-ups and shutdowns last for hours and do not typically give linear increases in temperature [30].

The material model utilized in this work does not account for microstructural changes caused by tempering (e.g. martensitic lath coarsening) which may influence constitutive response. It also does not address possible creep effects caused by exposure to high temperature for extended periods of time. The model only accounts for temperature and expansion. The key factor influencing the response in the current work was the temperature range rather than the heating-rate or possible dwells at high temperature. As a result, there was no advantage to simulating a realistic start-up cycle; hence, it was expedient to idealise the heating and cooling cycles as being of short duration.

The work presented here demonstrates key issues faced by modern power plant for load-following conditions. The ICHAZ is predicted to be a weaker region than the PM and the welded joint (CW specimen) is significantly weaker than the PM. The predicted WLRF is 4.5 although this may decrease with inclusion of PWHT effects. The value of 4.5 is significantly higher than previously reported experimental results for high temperature low cycle fatigue (HTLCF) of P91 welds at 400 ^{o}C and 500 ^{o}C [7] (Fig. 12). The TMF-induced accentuation of WLRF by a factor of about 1.33 is however consistent with previously reported values comparting TMF and HTLCF data at 600^{o}C [14]. The 'TMF-modified' result is shown in Fig 12.

This general modelling methodology presented here has been applied elsewhere to the HTLCF of CW P91 specimens, including the effects of PWHT [28]. The simulations were limited to short-term PWHT durations (up to 30 mins), for computational efficiency reasons, whereas the test data [31] was based on long term PWHT times of 180 mins; the predicted trend of effect of PWHT time, with extrapolation using a power-

law trend-line to the longer term, showed very close correlation (within 0.1%) to the experimental data (see Table 7), as shown in Fig. 17.

Future work will investigate more detailed validation of the present modelling methodology against experimental HTLCF and thermomechanical testing of CW and physically-simulated ICHAZ material. As the present model is based on dislocation density, the material model is considered to be key step towards understanding ICHAZ response. Future work will also implement more physically-based microstructure parameters such as Gibbs free energy to describe phase transformation (e.g. using ThermoCalc).

CONCLUSIONS

A through-process, physically-based, modified visco-plasticity model with damage has been developed for tempered, untempered and mixed-phase martensitic 9Cr steel material to represent the multi-axial thermo-mechanical behavior of heat-affected zone and parent 9Cr steel material, both during welding and post-weld.

The tempered martensite is seen to have significantly lower resistance to thermal cycling failure than the untempered material (more than 93% reduction) for the dislocation density and failure model implemented here. A higher yield stress in the low to medium temperature regime is predicted to be beneficial for thermal cyclic life.

Both tempered and untempered martensitic materials show significant notch sensitivity. A notch of 1% of specimen radius reduces life by about 80%.

A cross-weld specimen model, including parent material, ICHAZ and FGHAZ, predicted from a thermal analysis of the GTAW process, was shown to have significantly lower thermal cycling life than (i) either tempered or untempered martensite, and (ii) either 80% or 60% tempered martensite material (balance untempered). The reduction in life of the cross-weld specimen model is predicted to be similar to that of the notch cases investigated. This indicates that it is the heterogeneity of the mixture of the parent material, ICHAZ and FGHAZ that causes premature cracking.

ACKNOWLEDGMENT

The authors would like to acknowledge the contributors to this research; the National University of Ireland, Galway, the Ryan Institute, General Electric Alstom, ESB International, University of Limerick, Imperial College London and Fraunhofer IWM, Freiburg.

FUNDING

This research is funded by Science Foundation Ireland grant number SFI/14/IA/2604.

NOMENCLATURE

A_{c1}, A_{c3}	Austenitic start and finish temperatures for 9Cr steels (°C)
M_s, M_f	Martensitic start and finish temperatures for 9Cr steels (°C)
HAZ	Heat-affect zone
ICHAZ	Inter-critical HAZ
FGHAZ	Fine-grained HAZ
CGHAZ	Coarse-grained HAZ
GTAW	Gas tungsten are welding
PM	Parent material/metal
WM	Weld material/metal
PWHT	Post-weld heat treatment
CW	Cross-weld
CCT	Continuous-cooling-transformation
E	Young's Modulus (MPa)
G	Shear Modulus (MPa)
HTLCF	High temperature low cycle fatigue
σ_y	Yield stress (MPa)
T	Temperature (°C)
$\bar{\rho}$	Normalised dislocation density (-)
R	Taylor hardening (MPa)
V_f	Volume fraction
ρ_i	Initial dislocation density ($1/m^2$)
ρ	Current dislocation density ($1/m^2$)
c_1	Modelling constant (-)
c_2	Modelling constant (-)
α_g	Hardening constant (-)
M	Taylor factor (-)
b	Magnitude of burgers vector (m)
K	Recovery factor (-)
L	Dislocation mean path length (m)
B	Taylor hardening variable (MPa)
a_1	Modelling constant (-)
ω_1	Damage nucleation (-)
a_2	Modelling constant (-)
a_3	Modelling constant (-)
ω_2	Damage cavitation (-)
D	Damage (-)

α	Flow rule variable (1/s)
β	Flow rule variable (1/MPa)
φ_1	Flow rule variable (1/s)
φ_2	Flow rule variable (1/^{o}C)
φ_3	Flow rule variable (1/MPa)
φ_4	Flow rule variable (1/^{o}C)

REFERENCES

1. Potirniche, G., Charit, I., Rink, K., Barlow, F., *Prediction and monitoring systems of creep-fracture behaviour of 9Cr-1Mo steels for reactor pressure vessels.* NEUP 2009 Project, 2013. **09-835**.
2. Francis, J.A., Mazur, W., Bhadeshia, H. K. D. H.,, *Type IV cracking in ferritic power plant steels.* Materials Science and Technology, 2006. **22**(12): p. 1387-1395.
3. Ennis, P.J., Czyrska-Filemonowicz, A., *Recent Advances in Creep Resistant Steels for Power Plant Applications.* Operation Maintenance and Materials Issue, 2002. **1**(1).
4. Sauzay, M., Brillet, H., Monnet, I., Mottot, M., Barcelo, F., Fournier, B., Pineau, A., *Cyclically induced softening due to low-angle boundary annihilation in a martensitic steel.* Materials Science and Engineering A, 2005. **400-401**: p. 241-244.
5. Barrett, R.A., O'Donoghue, P. E., Leen, S. B., *A dislocation-based model for high temperature cyclic viscoplasticity of 9-12Cr steels.* Computational Materials Science, 2014. **92**: p. 286-297.
6. Hurtado-Norena, C., Danón, C. A., Luppo, M. I.,Bruzzoni, P., *Evolution of Minor Phases in a P91 Steel Normalized and Tempered at Different Temperatures.* Procedia Materials Science, 2015. **8**: p. 1089-1098.
7. Farragher, T.P., Scully, S., O'Dowd, N. P., Hyde, C. J., Leen, S. B., *High Temperature, low cycle fatigue characterisation of P91 weld and heat affected zone material.* Journal of Pressure Vessel Technology, 2014. **136**: p. 021403-1 - 021403-10.
8. Li, M., Barrett, R. A., Scully, S., Harrison, N. M., Leen, S. B., O'Donoghue, P. E.,, *Cyclic plasticity of welded P91 material for simple and complex power plant connections.* International Journal of Pressure Vessels and Piping, 2016. **87**: p. 391-404.
9. Divya, M., Das, C. R., Albert, S. K., Goyal, S., Ganesh, P., Kaul, R., Swaminathan, J., Murty, B. S., Kukreja, L. M., Bhaduri, A. K.,, *Influence of welding process on Type IV cracking behaviour of P91 steel.* Materials Science and Engineering A, 2014. **613**: p. 148-158.
10. Abe, F., Tabuchi, M., Tsukamoto, S., Shirane, T., *Microstructure evolutution in HAZ and suppression of Type IV fracture in advanced ferritic power plant steels.* International Journal of Pressure Vessels and Piping, 2010. **87**: p. 598-604.
11. Sawada, K., Hara., T., Tabuchi, M., Kimura, K., Kubushiro, K.,, *Microstructure characterisation of heat affected zone after welding in Mod.9Cr-1Mo steel.* Materials Characterisation, 2015. **101**: p. 106-113.
12. A. García-Junceda, C.C., F. G. Caballero, C. García de Andrés, *Dependence of martensite start temperature on fine austenite grain size.* Scripta Materialia, 2008. **58**: p. 134-137.
13. Abe, F., Tabuchi, M., Kondo, M., Tsukamoto, S., *Suppression of Type IV fracture and improvement of creep strength of 9Cr steel welded joints by boron addition.* International Journal of Pressure Vessels and Piping, 2007. **84**: p. 44-52.

14. Li, D.-F., Barrett, Richard A., O'Donoghue, Padraic E., Hyde, Chris J., O'Dowd, Noel P., Leen, Sean B., *Micromechanical finite element modelling of thermo-mechanical fatigue for P91 steels.* International Journal of Fatigue, 2016. **87**: p. 192-202.
15. Scully, S., *Personal correspondence.* ESB International, December 2018.
16. Yaghi, A.H., Hyde, T. H., Becker, A. A., Williams, J. A., Sun, W., *Residual stress simulation in welded sections of P91 pipes.* Journal of Materials Processing Technology, 2005. **167**: p. 480-487.
17. Yaghi, A.H., Hyde, T. H., Becker, A. A., Sun, W., *Finite element simulation of residual stresses induced by the dissimilar welding of a P92 steel pipe with weld metal IN625.* International Journal of Pressure Vessels and Piping, 2013. **111-112**: p. 173-186.
18. Mac Ardghail, P., Barrett, R. A., Harrison, N., Leen, S. B. *Towards a Through-Process model for welding of 9Cr steels*. in *10th International Conference on Trends in Welding Research, TWR 2016, & 9th International Welding Symposium of Japan Welding Society (9WS)*. 2016. Tokyo, Japan.
19. Tenaris, *Introduction to P91/T91 material*, in *International Workshop on Fabrication & Processing of Grade 91 Material, FAB 91*2011: Tiruchirappalli, India.
20. Vallourec & Mannesmann Tubes, *V & M Experience in T/P91 Tubes and Pipes*, in *International Workshop on Fabrication & Processing of Grade 91 Material, FAB 91*2011: Tiruchirappalli, India.
21. Li, H., Lin. J., Dean, T. A., Wen, S. W., Bannister, A. C., *Modelling mechanical property recovery of a linepipe steel in annealing process.* International Journal of Plasticity, 2009. **25**: p. 1049-1065.
22. Wei, X., Asgari, S. A., Wang, J. T., Rolfe, B. F., Zhu, H. C., Hodgson, P. D., *Micromechanical modelling of bending under tension forming behaviour of dual phase steel 600.* Computational Materials Science, 2015. **108**: p. 72-79.
23. Chaboche, J.L., *A review of some plasticity and viscoplasticity constitutive theories.* International Journal of Plasticity, 2008. **24**: p. 1642-1693.
24. Barrett, R.A., O'Donoghue, P. E., Leen, S. B., *A physically-based constitutive model for high temperature microstructural degredation under cyclic deformation.* International Journal of Fatigue, 2017. **100**: p. 388-406.
25. Lee, J.S., Maruyama, K., *Mechanism of Microstuctural Deterioration Preceding Type IV Failure in Weldment of Mod.9Cr-1Mo Steel.* Metallurgical Materials International, 2015. **21**: p. 639-645.
26. Hamelin, C.J., Muransky, O., Smith, M. C., Holden, T. M., Luzin, V., Bendeich, P. J., Edwards, L.,, *Validation of a numerical model used to predict phase distribution and residual stress in ferritic steel weldments.* Acta Materialia, 2014. **75**: p. 1-19.
27. Koistinen, D.P., Marburger, R.E, *A general equation prescribing the extent of the austenite-martensite transformation in pure iron-carbon alloys and plain carbon steels.* Acta Metallurgica, 1959. **7**(1): p. 59-60.
28. Mac Ardghail, P., Harrison, N., Leen, S. B., *A through-process, thermomechanical model for predicting welding-induced microstructure evolution*

and post-weld high-temperature fatigue response. International Journal of Fatigue, 2018. **112**: p. 216-232.
29. Rajan, T.V., Sharma, C. P., Sharma, A.,, *Heat Treatment Principles and Techniques*. 2nd ed2013: PHI Learning Private Limited.
30. Farragher, T.P., Scully, S., O'Dowd, N. P., Leen, S. B., *Development of life assessment procedures for power plant headers operated under flexible loading scenarios.* International Journal of Fatigue, 2013. **49**: p. 50-61.
31. Shankar, V., Sandhya, R., Mathew, M.D., *Creep-fatigue-oxidation interaction in Grade 91 steel weld joints for high temperature applications.* Materials Science and Engineering A, 2011. **528**: p. 8428-8437.

Figure Captions List

Fig. 1 Schematic CCT diagram for 9Cr steel, following [20].

Fig. 2 Contour plots of (a) post-weld distribution of tempered martensite PM (TMR volume fraction = 1) and untempered martensite (TMR volume fraction = 0) in a girth-weld simulation and (b) FE model of the simulated CW specimen (not to scale).

Fig. 3 Flowchart of the phase-evolution aspect of the through-process model.

Fig. 4 Flowchart of the mixed-phase constitutive aspect of the through-process model.

Fig. 5 Schematic of the axisymmetric cyclic out-of-phase thermo-mechanical simulation.

Fig. 6 Comparison between Abaqus UMAT (solid lines) and test data (symbols) at a range of temperatures for tempered martensite.

Fig. 7 Comparison between Abaqus UMAT (solid lines) and test data (symbols) at a range of temperatures for untempered martensite.

Fig. 8 Comparison of stress-temperature results for tempered and untempered martensite.

Fig. 9 Comparison of stress-temperature responses of ICHAZ (80% tempered martensite, 20% untempered martensite) with PM (Fully tempered)

Fig. 10 Effect of increasing volume fraction of untempered martensite on stress-temperature response, viz. PM (TMR1), ICHAZ (TMR80, TMR60) and

FGHAZ (UMR1)

Fig. 11 Comparison of cross-weld (CW) stress-temperature response with that of tempered PM

Fig. 12 Comparison of WLRF for isothermal HTLCF data [7], with projections forward to the peak temperature of this work. An adjusted WLRF based on TMF data [14] is also displayed.

Fig. 13 Effect of notch radius on tempered martensite stress-temperature response

Fig. 14 Effect of notch radius on untempered martensite stress-temperature response

Fig. 15 The evolution of the Von Mises stress, maximum in-plane principal strain and damage for the notched ($r_o/R = 0.25$) tempered martensite specimen at three points during the simulation.

Fig. 16 The evolution of the temperature, tempered martensite volume fraction and normalized dislocation density during welding-induced heating of the CW specimen.

Fig. 17 Model predictions [28] of the effect of PWHT (at 750^{o}C) time on HTLCF WLRF up to 30 min and a prediction of the WLRF at 180 min based on the trend set by the model predictions compared to HTLCF test data [31] (strain-range 2%, strain-rate 0.3%/s, 600^{o}C).

Table Caption List

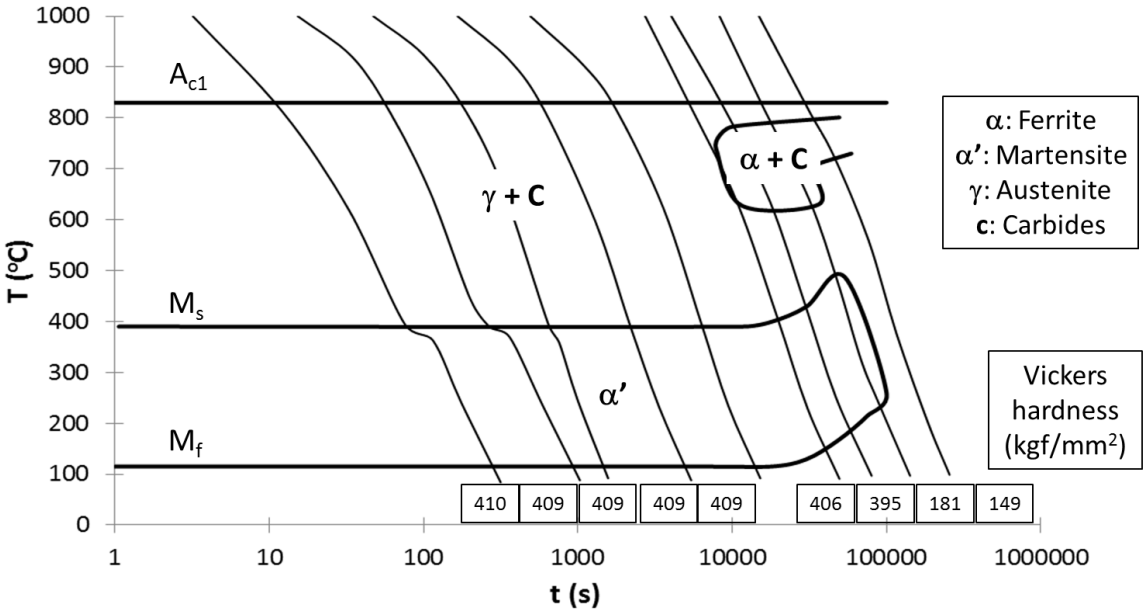
1000
900
800
700
600
500
400
300
200
100
0
T (°C)
A_{c1}
M_s
M_f
γ + C
α + C
α'
α: Ferrite
α': Martensite
γ: Austenite
c: Carbides
Vickers hardness (kgf/mm²)
410
409
409
409
409
406
395
181
149
1
10
100
1000
10000
100000
1000000
t (s)

Fig. 1

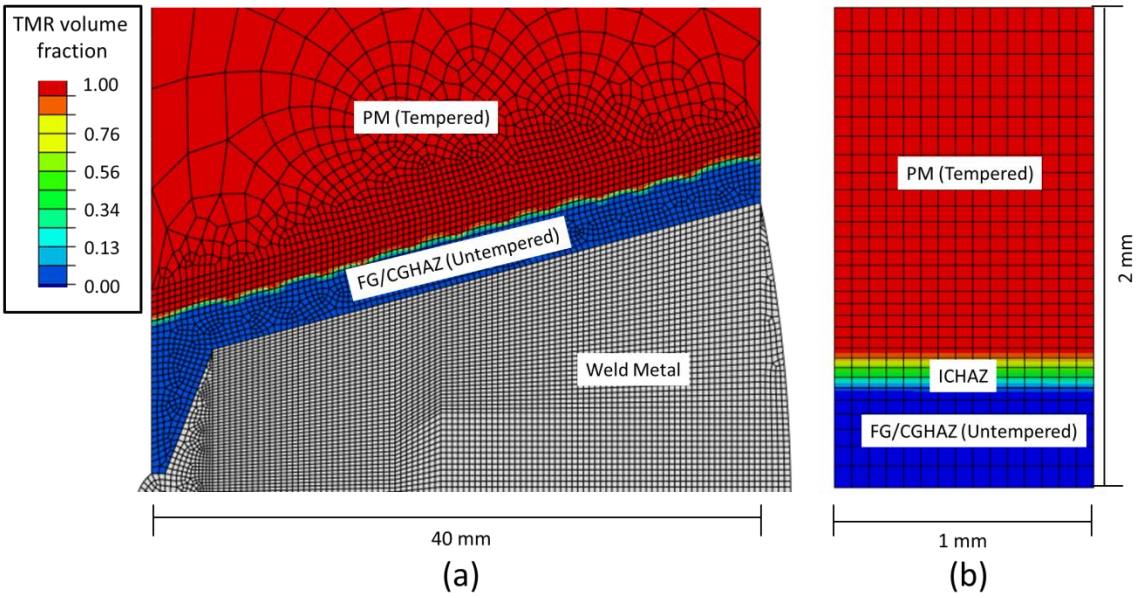
TMR volume fraction
1.00
0.76
0.56
0.34
0.13
0.00
PM (Tempered)
FG/CGHAZ (Untempered)
Weld Metal
40 mm
(a)
PM (Tempered)
ICHAZ
FG/CGHAZ (Untempered)
2 mm
1 mm
(b)

Fig. 2

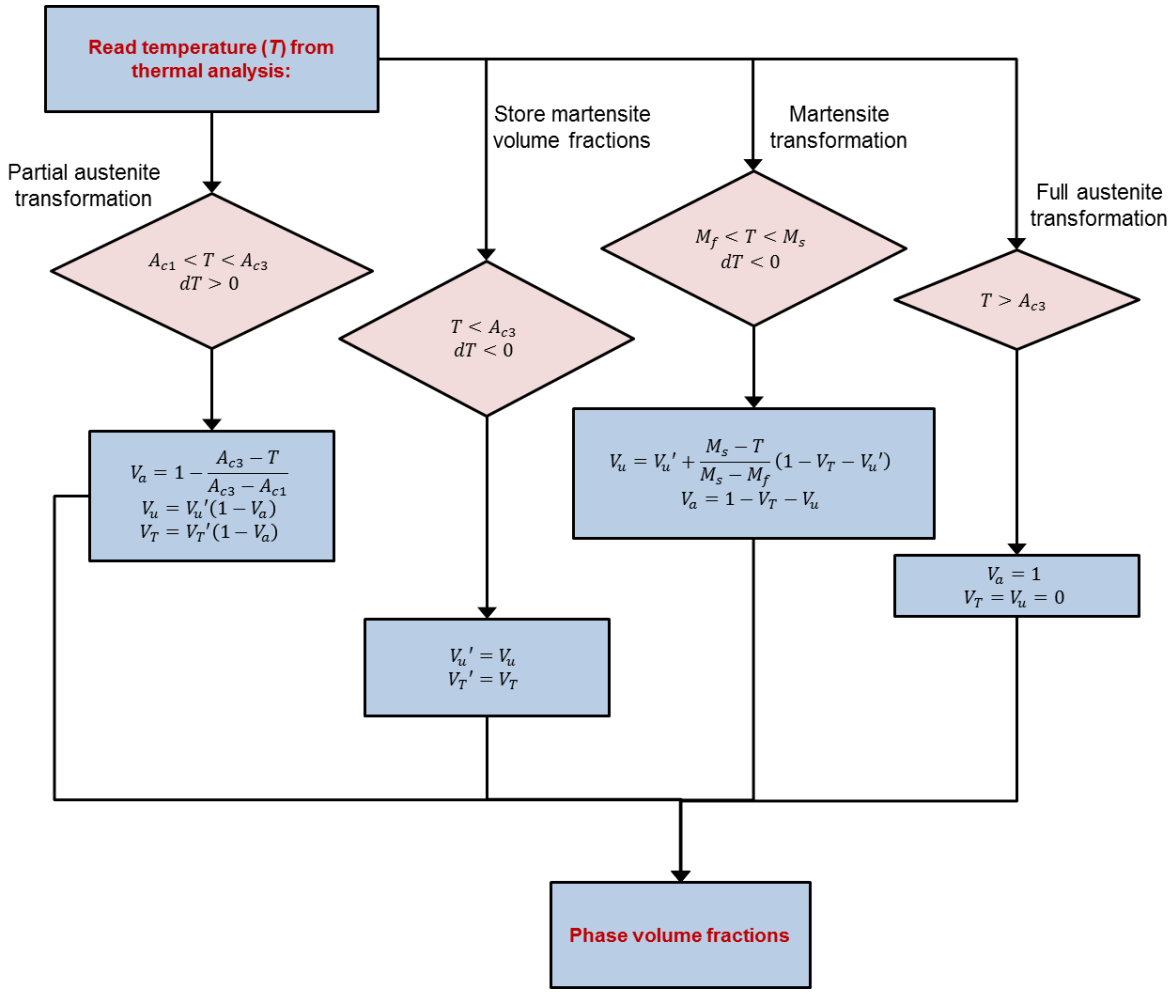
Read temperature (T) from thermal analysis:
Partial austenite transformation
$A_{c1} < T < A_{c3}$
$dT > 0$
$V_a = 1 - \frac{A_{c3} - T}{A_{c3} - A_{c1}}$
$V_u = V_u'(1 - V_a)$
$V_T = V_T'(1 - V_a)$
Store martensite volume fractions
$T < A_{c3}$
$dT < 0$
$V_u' = V_u$
$V_T' = V_T$
Martensite transformation
$M_f < T < M_s$
$dT < 0$
$V_u = V_u' + \frac{M_s - T}{M_s - M_f}(1 - V_T - V_u')$
$V_a = 1 - V_T - V_u$
Full austenite transformation
$T > A_{c3}$
$V_a = 1$
$V_T = V_u = 0$
Phase volume fractions

Fig. 3

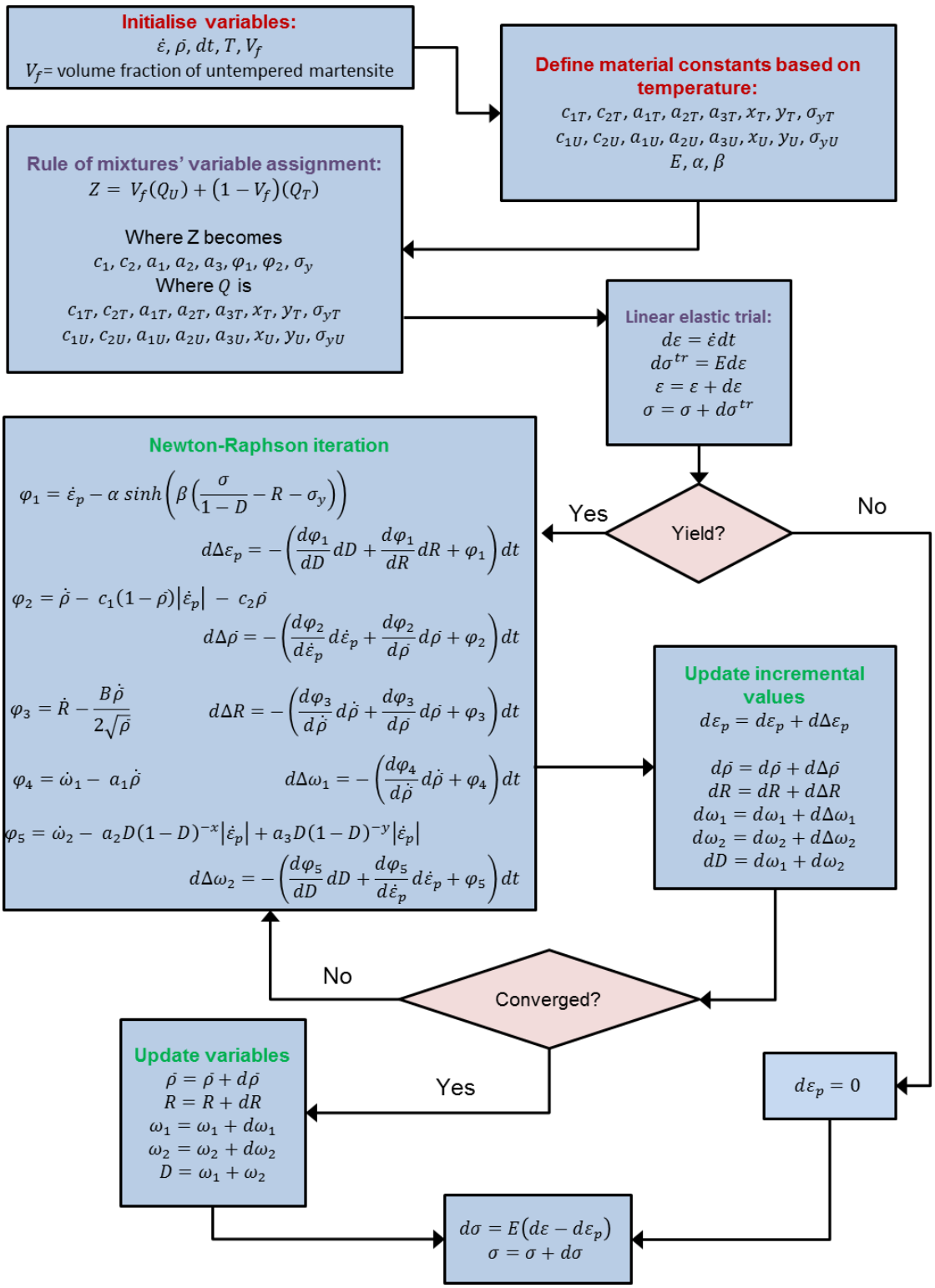
Initialise variables:
$\dot{\varepsilon}, \bar{\rho}, dt, T, V_f$
V_f= volume fraction of untempered martensite
Define material constants based on temperature:
$c_{1T}, c_{2T}, a_{1T}, a_{2T}, a_{3T}, x_T, y_T, \sigma_{yT}$
$c_{1U}, c_{2U}, a_{1U}, a_{2U}, a_{3U}, x_U, y_U, \sigma_{yU}$
E, α, β
Rule of mixtures' variable assignment:
$Z = V_f(Q_U) + (1 - V_f)(Q_T)$
Where Z becomes
$c_1, c_2, a_1, a_2, a_3, \varphi_1, \varphi_2, \sigma_y$
Where Q is
$c_{1T}, c_{2T}, a_{1T}, a_{2T}, a_{3T}, x_T, y_T, \sigma_{yT}$
$c_{1U}, c_{2U}, a_{1U}, a_{2U}, a_{3U}, x_U, y_U, \sigma_{yU}$
Linear elastic trial:
$d\varepsilon = \dot{\varepsilon} dt$
$d\sigma^{tr} = E d\varepsilon$
$\varepsilon = \varepsilon + d\varepsilon$
$\sigma = \sigma + d\sigma^{tr}$
Yield?
Yes
No
Newton-Raphson iteration
$\varphi_1 = \dot{\varepsilon}_p - \alpha \sinh\left(\beta\left(\frac{\sigma}{1-D} - R - \sigma_y\right)\right)$
$d\Delta\varepsilon_p = -\left(\frac{d\varphi_1}{dD} dD + \frac{d\varphi_1}{dR} dR + \varphi_1\right) dt$
$\varphi_2 = \dot{\bar{\rho}} - c_1(1-\bar{\rho})\left|\dot{\varepsilon}_p\right| - c_2\bar{\rho}$
$d\Delta\bar{\rho} = -\left(\frac{d\varphi_2}{d\dot{\varepsilon}_p} d\dot{\varepsilon}_p + \frac{d\varphi_2}{d\bar{\rho}} d\bar{\rho} + \varphi_2\right) dt$
$\varphi_3 = \dot{R} - \frac{B\dot{\bar{\rho}}}{2\sqrt{\bar{\rho}}}$
$d\Delta R = -\left(\frac{d\varphi_3}{d\dot{\bar{\rho}}} d\dot{\bar{\rho}} + \frac{d\varphi_3}{d\bar{\rho}} d\bar{\rho} + \varphi_3\right) dt$
$\varphi_4 = \dot{\omega}_1 - a_1\dot{\bar{\rho}}$
$d\Delta\omega_1 = -\left(\frac{d\varphi_4}{d\dot{\bar{\rho}}} d\dot{\bar{\rho}} + \varphi_4\right) dt$
$\varphi_5 = \dot{\omega}_2 - a_2 D(1-D)^{-x}\left|\dot{\varepsilon}_p\right| + a_3 D(1-D)^{-y}\left|\dot{\varepsilon}_p\right|$
$d\Delta\omega_2 = -\left(\frac{d\varphi_5}{dD} dD + \frac{d\varphi_5}{d\dot{\varepsilon}_p} d\dot{\varepsilon}_p + \varphi_5\right) dt$
Update incremental values
$d\varepsilon_p = d\varepsilon_p + d\Delta\varepsilon_p$
$d\bar{\rho} = d\bar{\rho} + d\Delta\bar{\rho}$
$dR = dR + d\Delta R$
$d\omega_1 = d\omega_1 + d\Delta\omega_1$
$d\omega_2 = d\omega_2 + d\Delta\omega_2$
$dD = d\omega_1 + d\omega_2$
Converged?
No
Yes
Update variables
$\bar{\rho} = \bar{\rho} + d\bar{\rho}$
$R = R + dR$
$\omega_1 = \omega_1 + d\omega_1$
$\omega_2 = \omega_2 + d\omega_2$
$D = \omega_1 + \omega_2$
$d\varepsilon_p = 0$
$d\sigma = E(d\varepsilon - d\varepsilon_p)$
$\sigma = \sigma + d\sigma$

Fig. 4

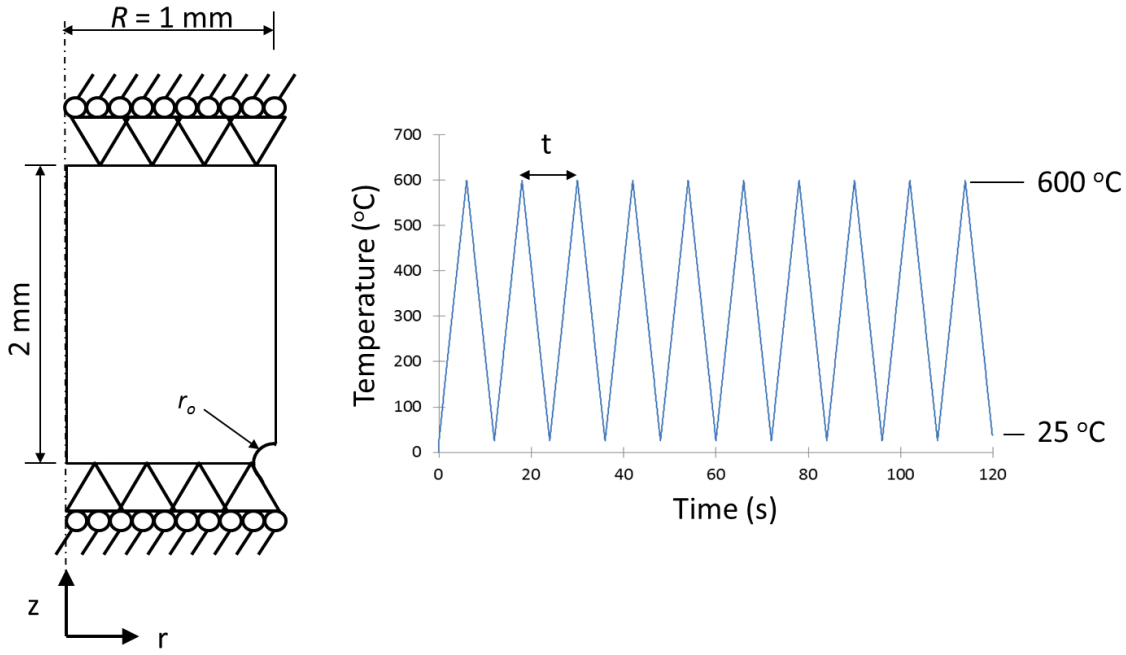
R = 1 mm
2 mm
r_o
z
r
t
Temperature (°C)
700
600
500
400
300
200
100
0
0
20
40
60
80
100
120
Time (s)
600 °C
25 °C

Fig. 5

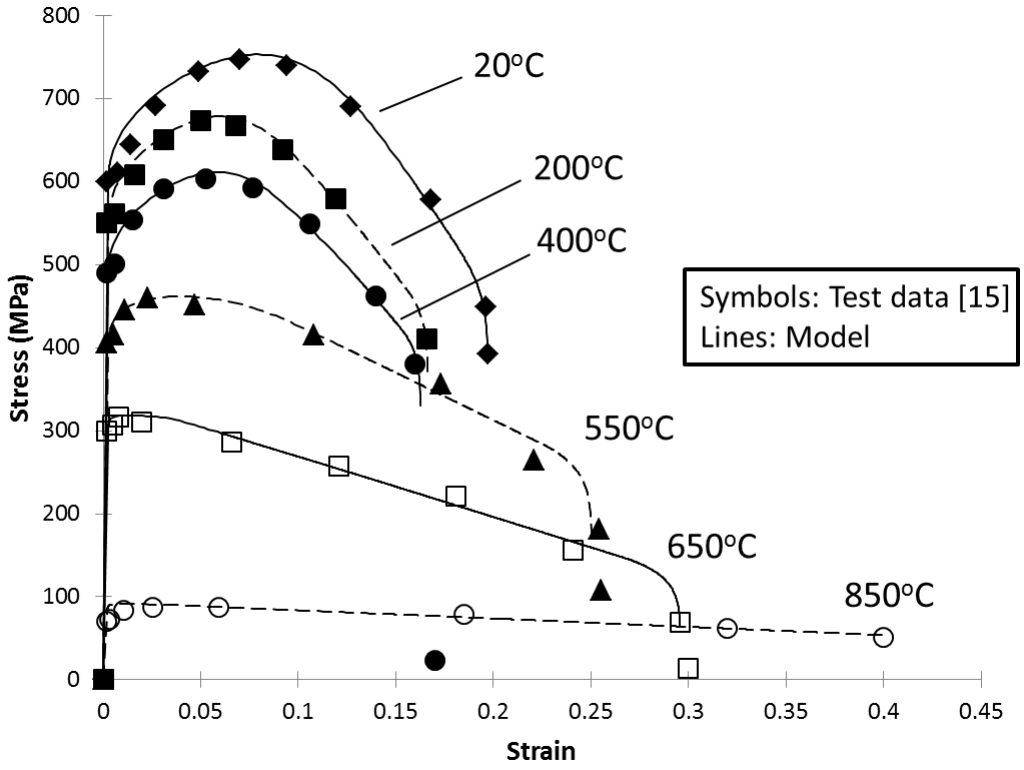
800
700
600
500
400
300
200
100
0
Stress (MPa)
0
0.05
0.1
0.15
0.2
0.25
0.3
0.35
0.4
0.45
Strain
20°C
200°C
400°C
550°C
650°C
850°C
Symbols: Test data [15]
Lines: Model

Fig. 6

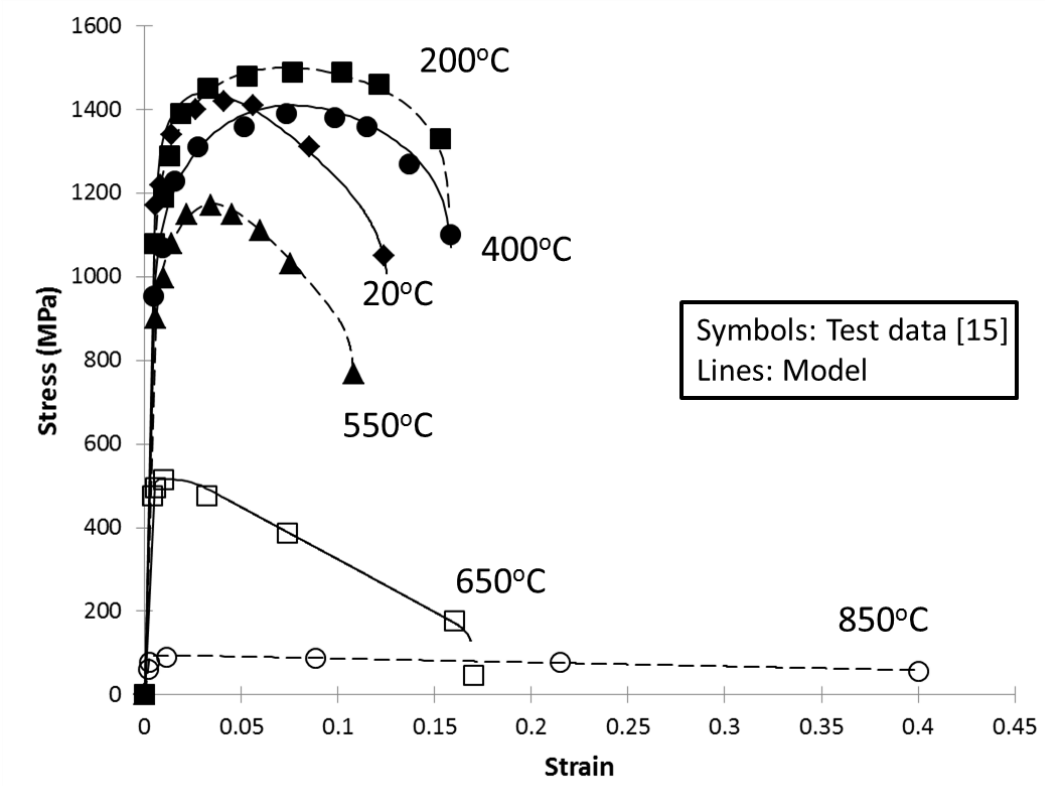
1600
1400
1200
1000
800
600
400
200
0
Stress (MPa)
0
0.05
0.1
0.15
0.2
0.25
0.3
0.35
0.4
0.45
Strain
200°C
400°C
20°C
550°C
650°C
850°C
Symbols: Test data [15]
Lines: Model

Fig. 7

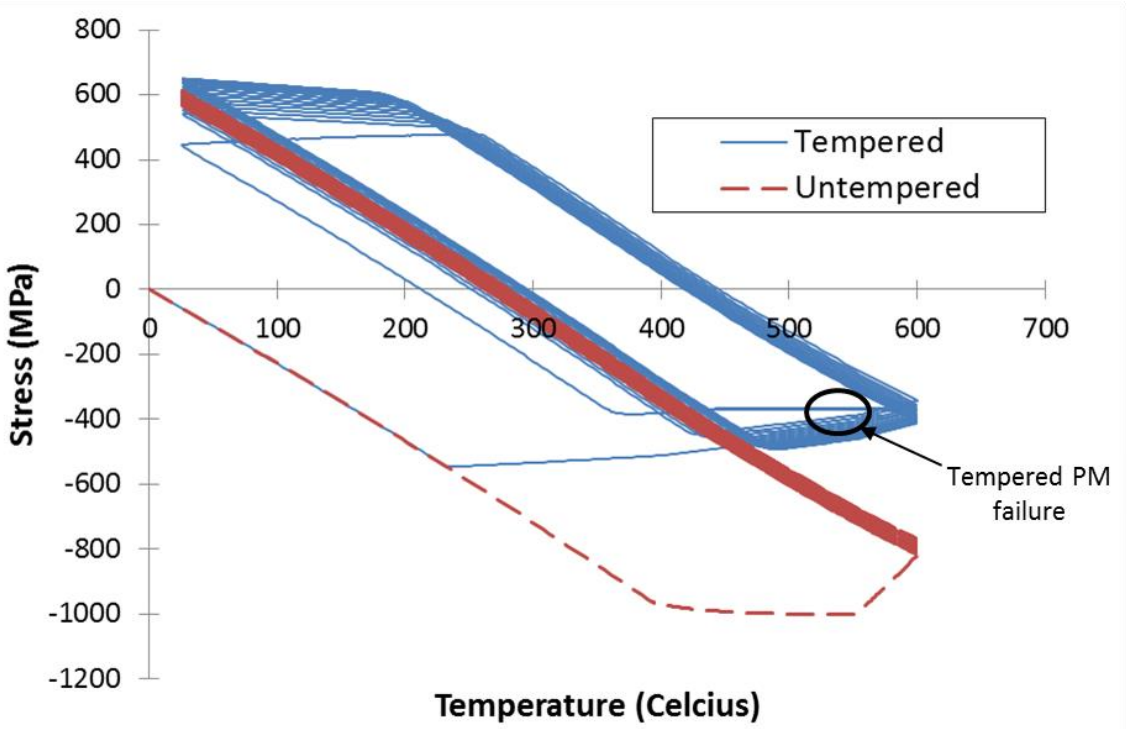
800
600
400
200
0
-200
-400
-600
-800
-1000
-1200
0
100
200
300
400
500
600
700
Stress (MPa)
Temperature (Celcius)
Tempered
Untempered
Tempered PM
failure

Fig. 8

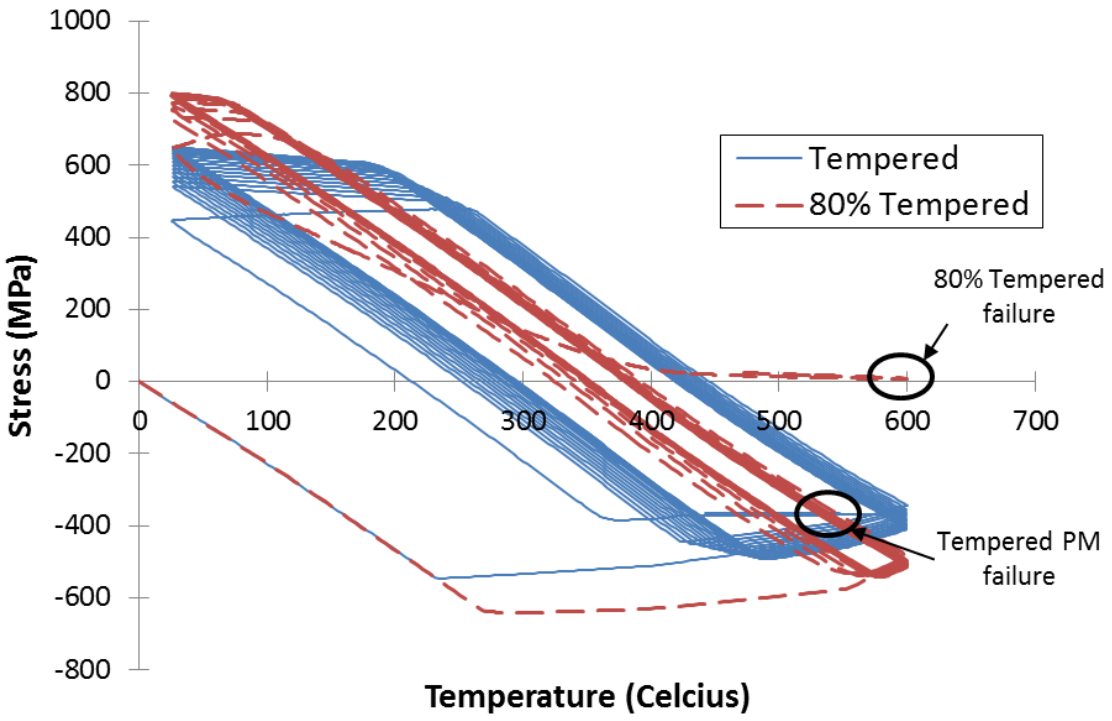
1000
800
600
400
200
0
-200
-400
-600
-800
0
100
200
300
400
500
600
700
Stress (MPa)
Temperature (Celcius)
Tempered
80% Tempered
80% Tempered failure
Tempered PM failure

Fig. 9

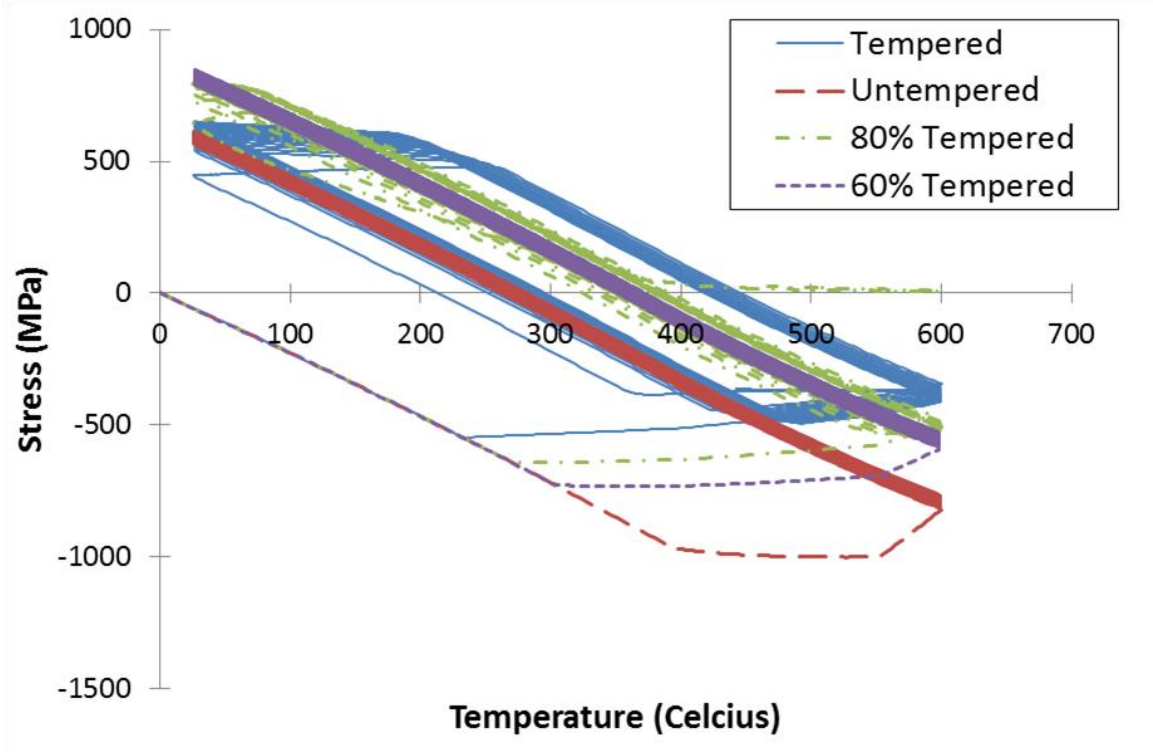
Tempered
Untempered
80% Tempered
60% Tempered
1000
500
0
-500
-1000
-1500
0
100
200
300
400
500
600
700
Stress (MPa)
Temperature (Celcius)

Fig. 10

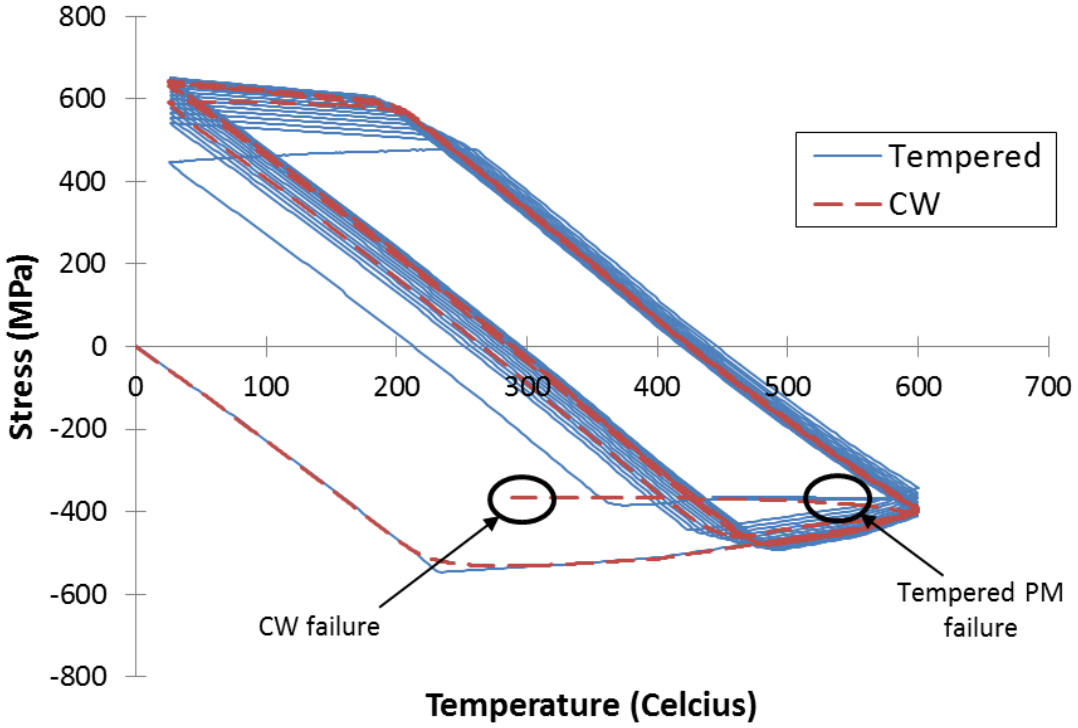
800
600
400
200
0
-200
-400
-600
-800
0
100
200
300
400
500
600
700
Stress (MPa)
Temperature (Celcius)
Tempered
CW
CW failure
Tempered PM
failure

Fig. 11

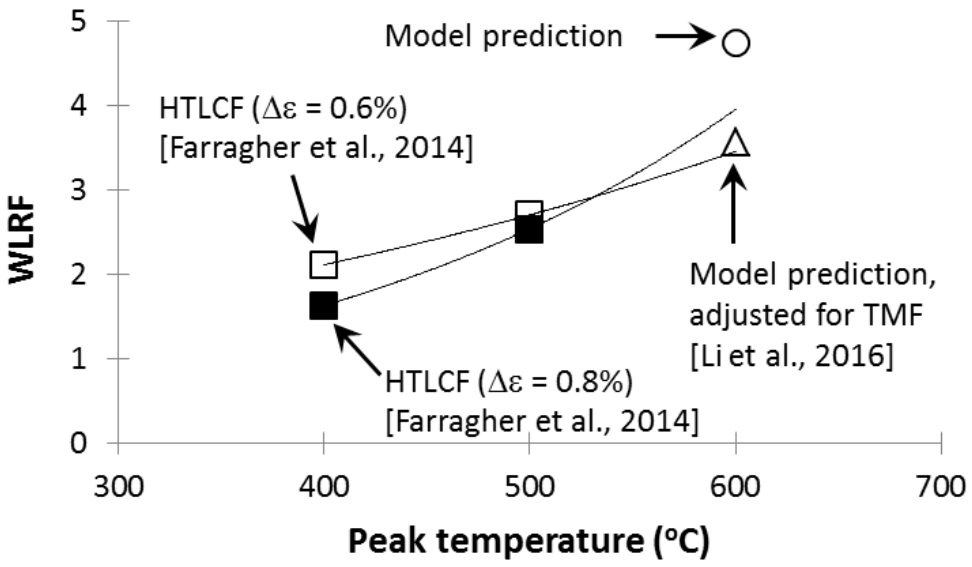
Model prediction
HTLCF (Δε = 0.6%)
[Farragher et al., 2014]
Model prediction,
adjusted for TMF
[Li et al., 2016]
HTLCF (Δε = 0.8%)
[Farragher et al., 2014]
WLRF
Peak temperature (°C)
0
1
2
3
4
5
300
400
500
600
700

Fig. 12

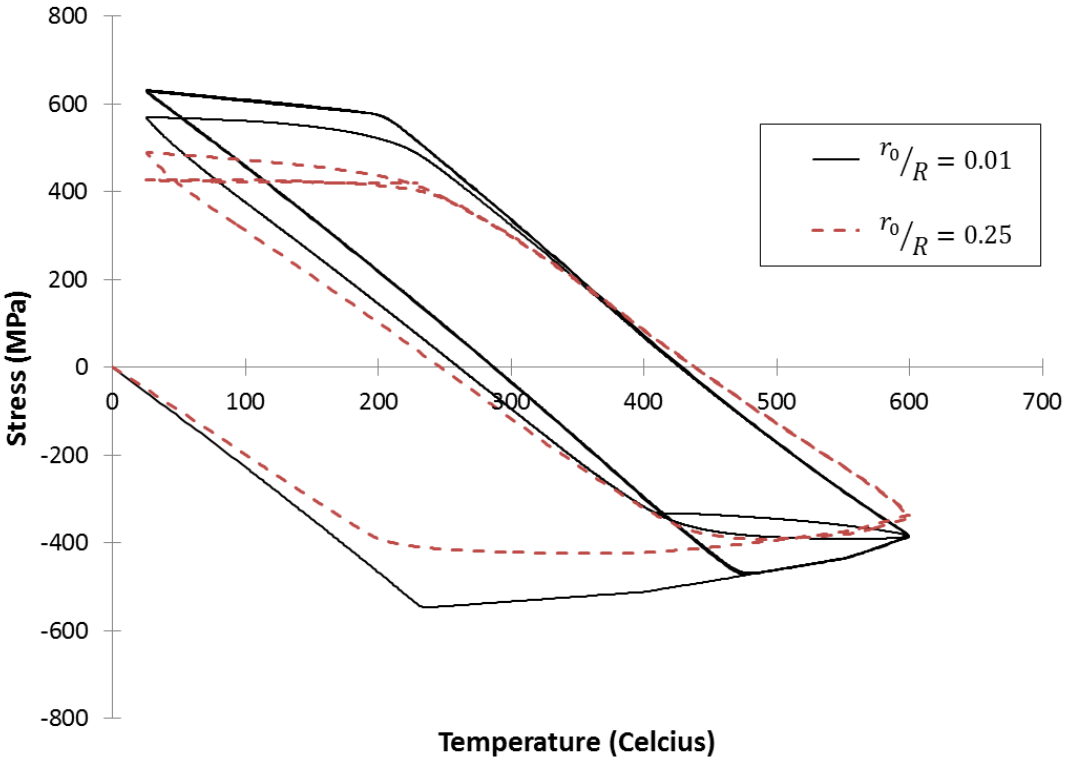
800
600
400
200
0
-200
-400
-600
-800
0
100
200
300
400
500
600
700
Stress (MPa)
Temperature (Celcius)
$r_0/_R = 0.01$
$r_0/_R = 0.25$

Fig. 13

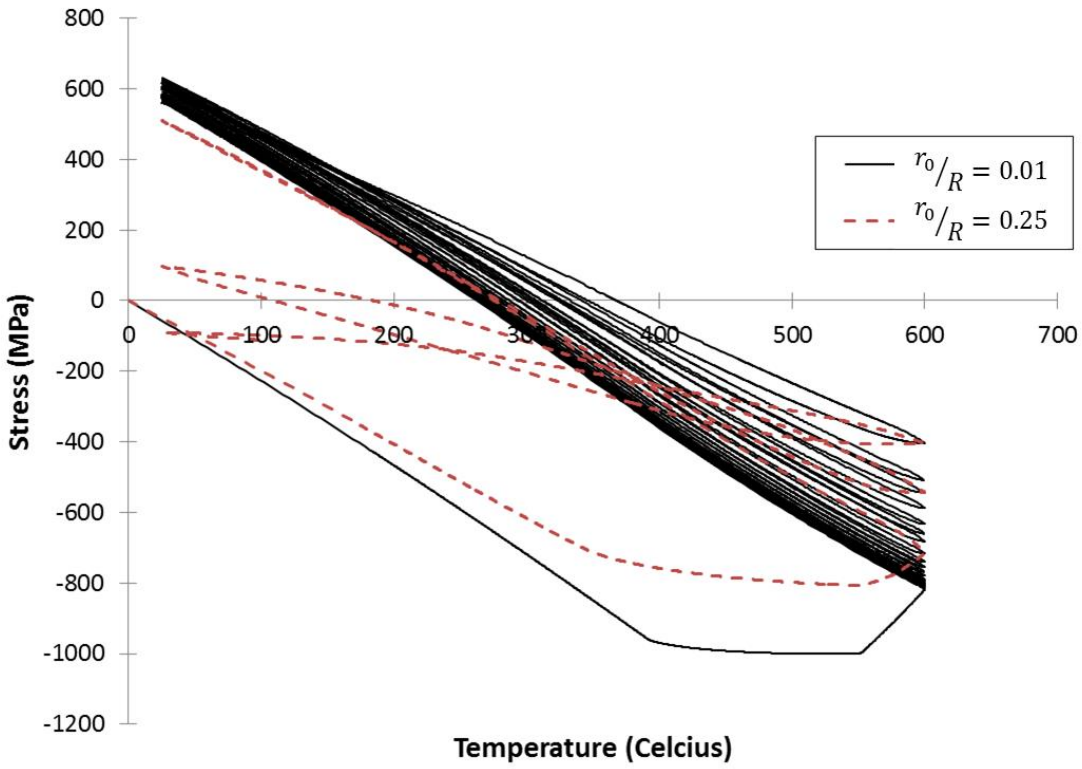
800
600
400
200
0
-200
-400
-600
-800
-1000
-1200
0
100
200
300
400
500
600
700
Stress (MPa)
Temperature (Celcius)
$r_0/R = 0.01$
$r_0/R = 0.25$

Fig. 14

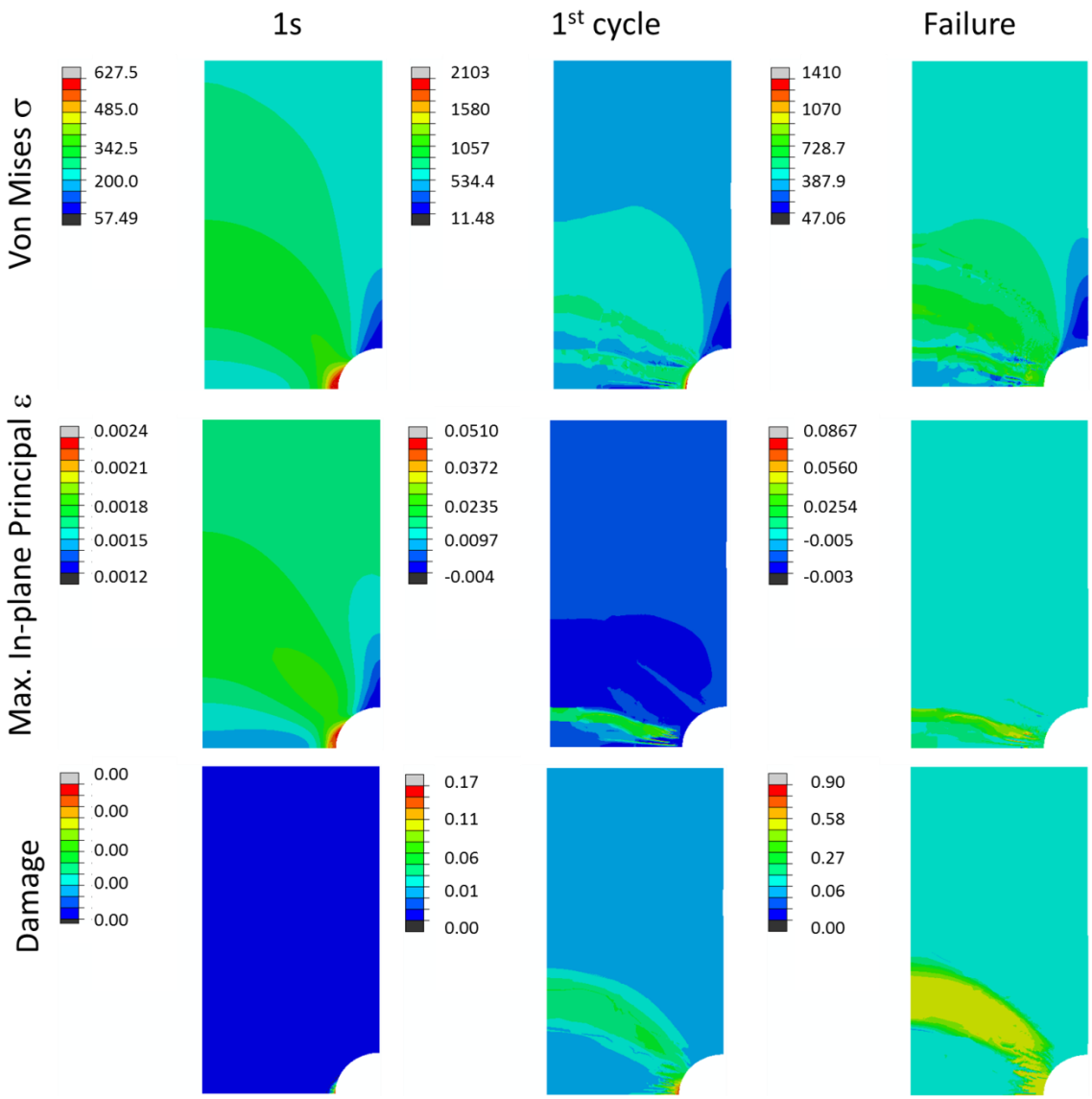
1s
1st cycle
Failure
Von Mises σ
627.5
485.0
342.5
200.0
57.49
2103
1580
1057
534.4
11.48
1410
1070
728.7
387.9
47.06
Max. In-plane Principal ε
0.0024
0.0021
0.0018
0.0015
0.0012
0.0510
0.0372
0.0235
0.0097
-0.004
0.0867
0.0560
0.0254
-0.005
-0.003
Damage
0.00
0.00
0.00
0.00
0.00
0.17
0.11
0.06
0.01
0.00
0.90
0.58
0.27
0.06
0.00

Fig. 15

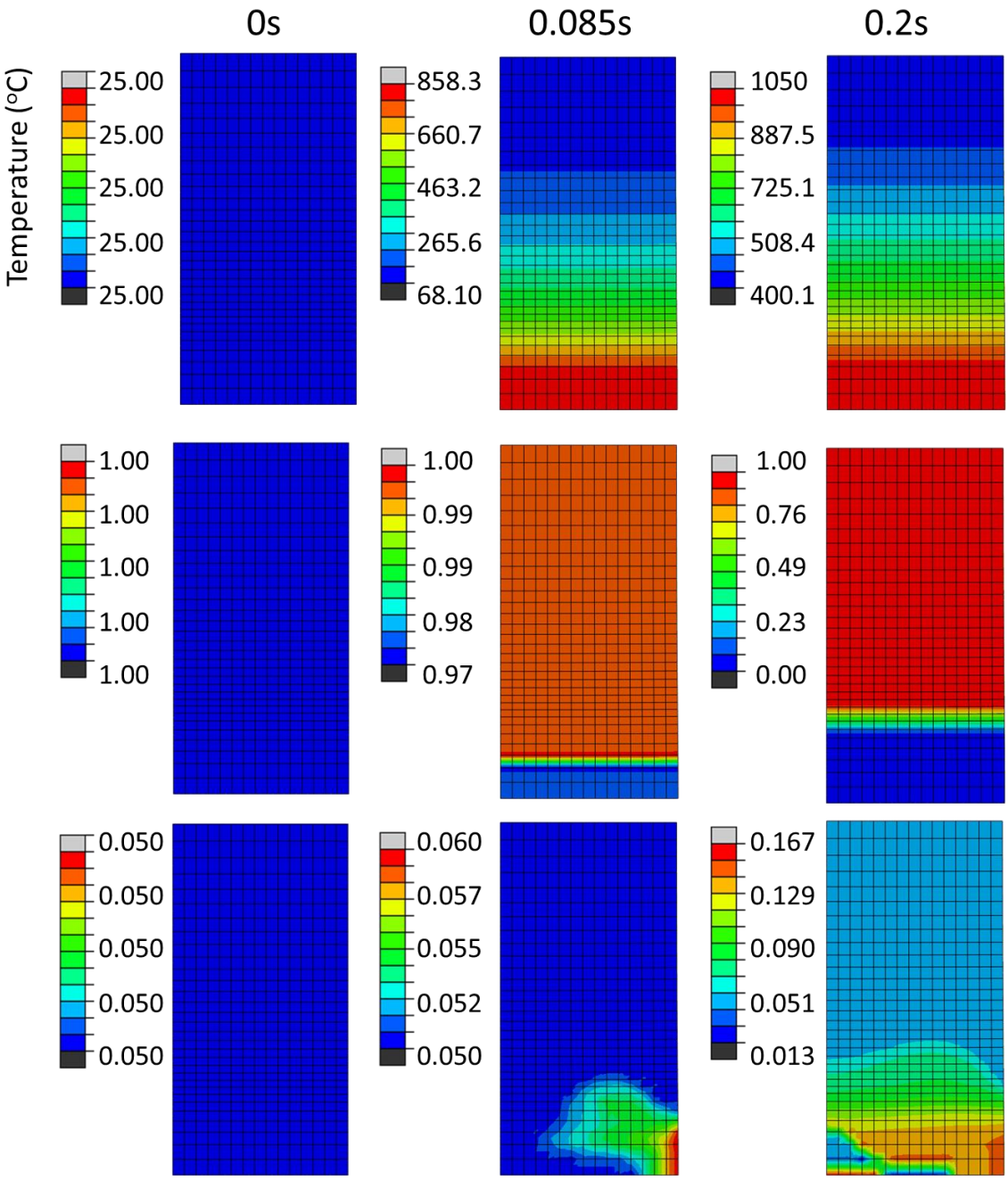
0s
0.085s
0.2s
Temperature (°C)
25.00
25.00
25.00
25.00
25.00
858.3
660.7
463.2
265.6
68.10
1050
887.5
725.1
508.4
400.1
1.00
1.00
1.00
1.00
1.00
1.00
0.99
0.99
0.98
0.97
1.00
0.76
0.49
0.23
0.00
0.050
0.050
0.050
0.050
0.050
0.060
0.057
0.055
0.052
0.050
0.167
0.129
0.090
0.051
0.013

Fig. 16

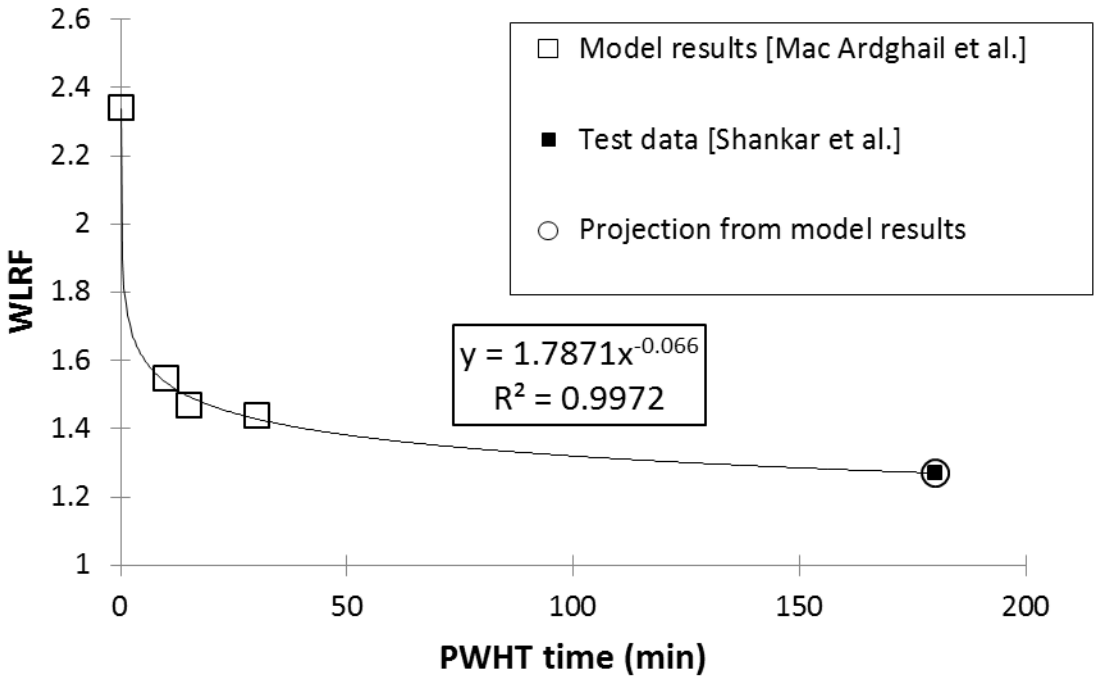
Model results [Mac Ardghail et al.]
Test data [Shankar et al.]
Projection from model results
y = 1.7871x-0.066
R² = 0.9972
WLRF
PWHT time (min)
2.6
2.4
2.2
2
1.8
1.6
1.4
1.2
1
0
50
100
150
200

Fig. 17

A_{c1}	A_{c3}	M_s	M_f
830°C [17]	920°C [17]	400°C [20]	100°C [20]

Table.1

α_g (-)	b (mm)	M (-)	K (1/mm)	L (mm)
0.33	0.25×10^{-6}	3	41	3.8×10^{-5}

Table.2

Name	Description	Notch details	Cycles to failure
Case 1	PM, tempered martensite	N/A	19
Case 2	PM, tempered martensite	r_o/R = 0.01	4
Case 3	PM, tempered martensite	r_o/R = 0.25	2
Case 4	ICHAZ, 80% tempered martensite	N/A	14
Case 5	ICHAZ, 60% tempered martensite	N/A	>150 (ES)
Case 6	Untempered martensite	N/A	>300 (ES)
Case 7	Untempered martensite	r_o/R = 0.01	40
Case 8	Untempered martensite	r_o/R = 0.25	3
Case 9	Cross-weld	N/A	4

Note: ES = elastic shakedown

Table.3

T (°C)	E (GPa)	σ_y (MPa)	c_1 (-)	c_2 (-)	a_1 (-)	a_2 (-)	a_3 (-)	x (-)	y (-)
20	215	1170	9	0	0.6	0.5	0.0005	-3	-15.5
200	207	1080	9	0	0.3	1.2	0.03	-3	-15.5
400	198	954	9	0	0.2	7	0.03	0	-15
550	156	900	9	0	0.1	80	0.03	6.2	-11.7
650	114	475	9	2	0.1	120	0.03	15	-5
850	40.2	85	9	10	0.1	200	0.03	75	-5

Table.4

T (°C)	E (GPa)	σ_y (MPa)	c_1 (-)	c_2 (-)	a_1 (-)	a_2 (-)	a_3 (-)	x (-)	y (-)
20	215	600	0.4	0	0.3	35	0.0005	2.5	-15.5
200	207	550	0.4	0	0.3	52	0.0012	4	-15.5
400	198	490	0.4	0	0.3	55	0.0012	4.2	-15.5
550	156	406	0.4	0.07	0.3	55	0.1	8	-8
650	114	300	0.4	0.7	0.3	160	0.1	24	-4.9
850	40.2	83	0.4	0.7	0.3	150	0.1	50	-4.9

Table.5

φ_1 (1/s)	φ_2 (1/°C)	φ_3 (1/MPa)	φ_4 (1/°C)
0.000256	0.00194	0.2428	-0.00059

Table.6

PWHT time (min)	WLRF	Detail
180	1.27	Test data [31]
0	2.34	Model results [28]
10	1.55	
15	1.47	
30	1.44	
180	1.269	Projection from model results

Table 7.